

Light–Matter Interaction in Quantum Confined 2D Polar Metals

Katharina Nisi, Shruti Subramanian, Wen He, Kanchan Ajit Ulman, Hesham El-Sherif, Florian Sigger, Margaux Lassaunière, Maxwell T. Wetherington, Natalie Briggs, Jennifer Gray, Alexander W. Holleitner, Nabil Bassim, Su Ying Quek, Joshua A. Robinson,* and Ursula Wurstbauer**

This work is a systematic experimental and theoretical study of the in-plane dielectric functions of 2D gallium and indium films consisting of two or three atomic metal layers confined between silicon carbide and graphene with a corresponding bonding gradient from covalent to metallic to van der Waals type. *k*-space resolved free electron and bound electron contributions to the optical response are identified, with the latter pointing towards the existence of thickness dependent quantum confinement phenomena. The resonance energies in the dielectric functions and the observed epsilon near-zero behavior in the near infrared to visible spectral range, are dependent on the number of atomic metal layers and properties of the metal involved. A model-based spectroscopic ellipsometry approach is used to estimate the number of atomic metal layers, providing a convenient route over expensive invasive characterization techniques. A strong thickness and metal choice dependence of the light–matter interaction makes these half van der Waals 2D polar metals attractive for quantum engineered metal films, tunable (quantum-)plasmonics and nano-photonics.

1. Introduction

Understanding the interaction between light and matter is a continuously evolving discipline with high technological relevance, including but not limited to the fields of bio-medical engineering, communication, energy conversion, sensing, computation, cryptography, and quantum technologies. Central to all optical technologies is the manipulation of the light–matter interaction to achieve a high level of control, particularly in technologically relevant solid-state nanomaterials with functionality in a large wavelength range—near infrared (NIR) to visible and ultraviolet (UV) regions. The weak interaction of this large wavelength range of light with


K. Nisi, M. Lassaunière, Prof. U. Wurstbauer
Institute of Physics
University of Münster
48149 Münster, Germany
E-mail: wurstbauer@www.de

K. Nisi, F. Sigger, Prof. A. W. Holleitner
Walter Schottky Institute
Technical University of Munich
85748 Garching, Germany

K. Nisi, F. Sigger, Prof. A. W. Holleitner
Physics Department
Technical University of Munich
85748 Garching, Germany

Dr. S. Subramanian, M. T. Wetherington, N. Briggs, Prof. J. A. Robinson
Department of Materials Science and Engineering
The Pennsylvania State University
University Park, PA 16802, USA
E-mail: jrobinson@psu.edu

Dr. S. Subramanian, M. T. Wetherington, N. Briggs, Prof. J. A. Robinson
Center for 2D and Layered Materials
The Pennsylvania State University
University Park, PA 16802, USA

 The ORCID identification number(s) for the author(s) of this article can be found under <https://doi.org/10.1002/adfm.202005977>.

© 2020 The Authors. Published by Wiley-VCH GmbH. This is an open access article under the terms of the Creative Commons Attribution License, which permits use, distribution and reproduction in any medium, provided the original work is properly cited.

DOI: 10.1002/adfm.202005977

W. He
Department of Materials Science and Engineering
National University of Singapore
9 Engineering Drive 1, Singapore 117575, Singapore

W. He, K. A. Ulman, Prof. S. Y. Quek
Centre for Advanced 2D Materials
National University of Singapore
6 Science Drive 2, Singapore 117546, Singapore
E-mail: phyqsy@nus.edu.sg

H. El-Sherif, Prof. N. Bassim
Department of Materials Science and Engineering
McMaster University
1280 Main St W, Hamilton, ON L8S 4L8, Canada

M. T. Wetherington, J. Gray
Materials Research Institute
The Pennsylvania State University
University Park, PA 16802, USA

Prof. S. Y. Quek
Department of Physics
National University of Singapore
Singapore 117551, Singapore

N. Briggs, Prof. J. A. Robinson
2D Crystal Consortium
The Pennsylvania State University
University Park, PA 16802, USA

Prof. J. A. Robinson
Center for Atomically Thin Multifunctional Coatings
The Pennsylvania State University
University Park, PA 16802, USA

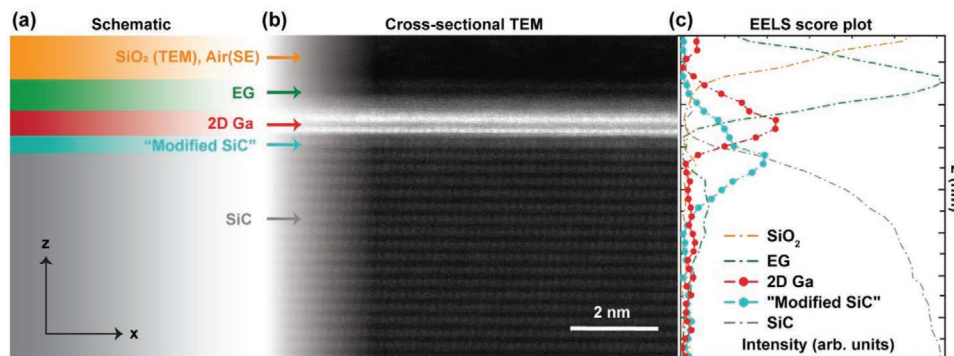


Figure 1. a) Schematic of the layered 2D metal heterostack. b) High-resolution cross-sectional transmission electron micrograph of the graphene/2D Ga/SiC heterostack. Encapsulation of the 2D metal between epitaxially grown graphene and SiC substrate, allows for environmental stability and its characterization outside of UHV conditions. The two atomic layers of Ga show up with brighter contrast in the transmission electron micrograph. c) Multivariate analysis of the EELS map reveals five unique components and the score plot intensity for each component are shown along the z-direction of the TEM cross-section. This EELS score plot reveals a 1–2 nm thick modified SiC peak that shows up at the interface of the 2D Ga and the SiC substrate.

solids necessitates the development of approaches to enhance and controllably manipulate the light–matter interaction. One such approach is the investigation of near-zero index (NZI) materials for nano-plasmonics or nano-photonics.^[1–6] Epsilon near-zero (ENZ) materials are a class of NZI materials that exhibit unique properties such as vanishing group-velocity, giant field enhancement, static light, decoupling of spatial and temporal field variations, light tunneling, and extreme non-linear interactions.^[4,7–13] Access to these field dynamics and tunable properties allows for the design of unconventional photonic and plasmonic devices using ENZ materials.^[11,12,14–31] ENZ materials with high losses are not suitable for applications using the slow light and wavelength expansion properties,^[4,14] but suitable for applications using confinement and impedance effects.^[4] Potential applications for ENZ materials with high losses include optical absorbers, for generating hot-electrons, or for nanoparticle trapping.^[4] Both structured and homogenous ENZ materials have been extensively studied. Structured ENZ materials offer high tunability, but their complex fabrication is expensive. The family of homogenous ENZ materials encompasses metals, semi-metals, doped semiconductors and interband materials, which allow for easy integration with other nano-photonics elements like single photon emitters and wave-guides.^[32] Bulk metals with plasmon frequencies in the ultraviolet to visible spectral range are commonly studied, but they miss out on the telecommunication wavelengths, possess low tunability via gating, straining, and suffer from high losses.^[4] Reduced losses have been theoretically predicted for ultrathin metallic films.^[33–37] Such thin metallic films are also of interest in the field of quantum plasmonics^[38] and to study and tailor the quantum physical properties of thin metals.^[39] Slow plasmons and giant field enhancement have been theoretically shown for atomically thin quasi 2D metals.^[40] Although gate tunable ultrathin gold films have recently been realized,^[41] the fabrication of ultrathin 2D metals and other small-band gap systems remains challenging, and these materials are prone to interfacial environmental degradation.

Recently, 2D polar metals were realized via confinement heteroepitaxy (CHet)—a process of intercalating metals between

epitaxially grown graphene and its silicon carbide (SiC) substrate (Figure 1).^[42] These 2D gallium (Ga) and 2D indium (In) structures are protected by the graphene overlayers, demonstrate a gradient in their bonding covalency along the z-direction, and exhibit fascinating properties like superconductivity,^[42] strong plasmonic response in the visible range,^[43] and strong nonlinear optical properties emerging by giant second harmonic generation in the NIR range approaching $10 \text{ nm}^2 \text{ V}^{-1}$.

In this study, we explore the linear optical response of 2D Ga and 2D In. The fundamental light–matter interaction which is described by the complex dielectric functions. We determine the dielectric functions of 2D Ga and 2D In via a combination of spectroscopic ellipsometry (SE) and density functional theory (DFT) in a large spectral range from NIR to UV. We are able to distinguish between the free and bound electron contributions to the optical response. In addition to an expected ENZ region around the plasmon frequency of free electrons in the UV spectral range, a pronounced ENZ region is observed in the visible to NIR spectral range for these 2D metals. A comparison can be drawn between the quantized bound electron transitions in bilayer and trilayer 2D metals,^[44] and thickness dependent eigen energy states in quantum wells. The imaginary part of the dielectric functions coupled with DFT calculations allows for the determination of the number of atomic metal layers. The studied samples consist of predominantly homogenous bilayer 2D Ga, and a mixture of bilayer and trilayer 2D In with approximately 66% bilayer (see Section S1, Supporting Information). The characteristic signatures for bi- and trilayer 2D metal films and their variation between Ga and In suggest tunability of the ENZ region by quantum confinement (number of layers and atomic radii), atomic number, and potentially by alloying and external stimuli such as gating. The half van der Waals nature of 2D metals facilitates their combination with other 2D or low dimensional structures as well as photonic or plasmonic circuitries, making them especially interesting for next generation photonics, quantum plasmonics, quantum technologies, hot-electron generation, photo-catalysis, solar power harvesting, sensing, and nanoparticle trapping.^[38,41,45–50]

2. Results and Discussion

2.1. Spectroscopic Ellipsometry

Ellipsometry is a non-destructive, optical method that measures the change in the polarization of collimated monochromatic light being reflected from thin films at a finite angle of incidence as schematically shown in Figure 2a. We use SE in reflectance geometry, where light from a tunable source is guided through a polarizer for linear polarization, and then through a compensator to prepare elliptically polarized light. The reflected light is directed to the detector through an analyzer. In a suitable coordinate system, the complex reflectance matrix is described by $\rho = r_p/r_s = \tan\Psi \cdot e^{i\Delta}$, where ρ is the complex reflectance ratio, r_p and r_s are the amplitudes of the parallel (p) and orthogonal (s) components of the reflected light normalized to the amplitude of incoming light, Ψ and Δ are the ellipsometric angles.^[51] In our 2D metal heterostacks, the complex dielectric function $\varepsilon(\omega) = \varepsilon_1(\omega) + i\varepsilon_2(\omega)$ is dominated by the isotropic in-plane contribution $\varepsilon^{xx}(\omega)$, and layer thickness d of the thin films constituting the layer stack. We perform variable angle spectroscopic ellipsometry (VASE) measurements, and spectroscopic imaging ellipsometry (SIE) to obtain high lateral resolution (results shown in Section S2, Supporting Information).^[51,52] For the VASE measurements, the entire sample is illuminated with collimated monochromatic light with a spectral range of 300–1700 nm under three angles of incidence

(AOI)—55°, 60°, and 65°, and subsequent regression analysis to extract the dielectric functions from the measured $\Psi(\omega)$ and $\Delta(\omega)$.

To describe the VASE and SIE spectra of the 2D polar metals and extract their dielectric functions, a comprehensive optical model is developed and fit to the experimental data via regression analysis. To minimize the number of unknown parameters, quasi-free-standing hydrogen intercalated epitaxial graphene (QFEG)^[53,54] is measured and modeled separately to determine dielectric functions and optically active film thickness of epitaxial graphene and the SiC substrate. These parameters are then used as input to model the VASE and SIE spectra of the full heterostack comprised of (from bottom to top) the SiC substrate, thin modified SiC, 2–3 atomic layers of metal, QFEG, and air as shown in Figure 1a. The dielectric function of QFEG is determined by modeling $\Delta(\omega)$ and $\Psi(\omega)$ with a Drude term for the free electrons in the graphene, and SiC is modeled using a Cauchy function.^[52,55,56] To model the ellipsometric $\Psi(\omega)$ and $\Delta(\omega)$ spectra of the 2D metal films, a Drude function is used to describe the free electron contribution to $\varepsilon(\omega)$ due to intraband excitations, Tauc-Lorentz and Lorentz functions are used to describe the bound electron contributions to $\varepsilon(\omega)$ due to interband excitations. A Cauchy-modeled intermediate layer, labeled modified SiC, is introduced to model the changes in the top few atomic layers of the SiC substrate during the EG growth and subsequent intercalation processes. The ellipsometric phase shift described by Δ is very sensitive to surface roughness and materials with finite refractive index

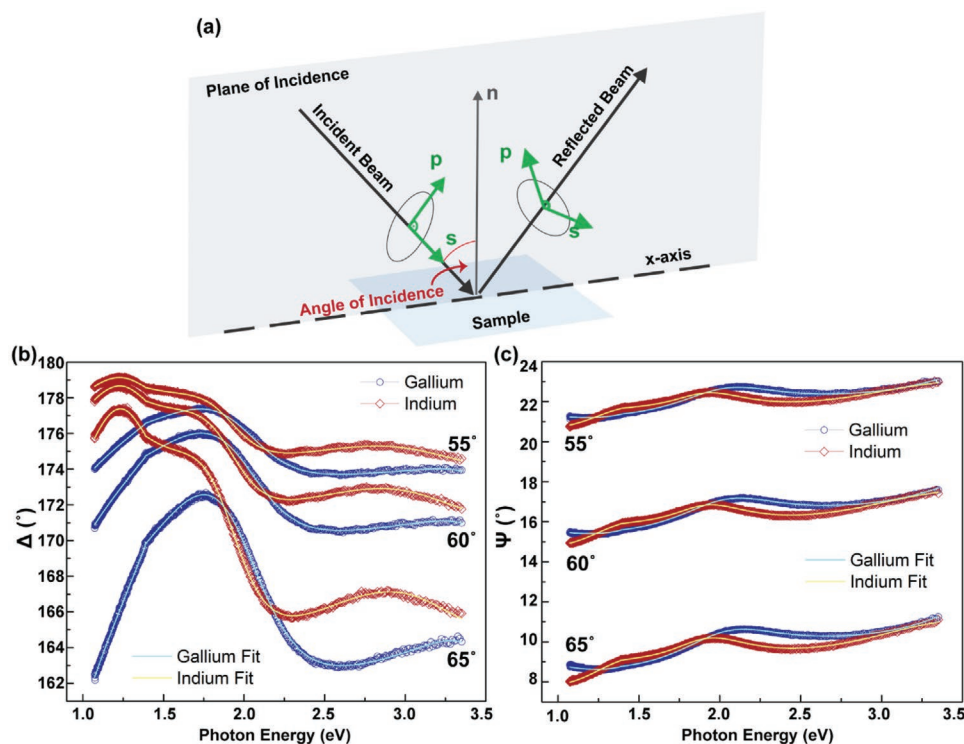


Figure 2. a) Schematic of the polarization state and geometry of light reflected from a thin film sample in VASE. b,c) The obtained ellipsometric angles, Δ and Ψ , respectively, for 2D Ga and 2D In at three different angles of incidence—55°, 60°, and 65°. SE was realized using an M-2000 ellipsometer (J. A. Woollam) in RCE-mode. The data was obtained in a spectral range of 300–1700 nm, that is, 0.73–4.13 eV. The blue and red curves show the fit obtained from the model for the 2D Ga and 2D In heterostacks, respectively. A Drude–Lorentz model is developed to fit the 2D metals.

Table 1. Overview of the materials in the 2D metal heterostack (as shown in Figure 1a) including the model contributions to the total function and the respective parameters.

Metal	Model	Parameters
Air	n, k fix	n, k
Graphene	Drude	E_0 [eV]; damping Γ_{graphene} [eV]
Gallium/Indium	Drude	E_0 [eV]; damping Γ_{Drude} [eV]
	Tauc–Lorentz	A [eV]; E_0 [eV]; Γ_{TL} [eV]; E_g [eV]
	Lorentz	Frequency [eV]; strength [eV ²]; damping [eV]
SiC	Cauchy	A_n, B_n [nm ²]

vanishing absorbance (e.g., insulating materials), and a constant offset of this angle to the model was observed when the modified SiC layer was not accounted for.^[57] The first few atomic layers of SiC are altered during the synthesis of graphene via silicon sublimation, which is readily identified by a modified contrast in the bulk SiC substrate at the metal/substrate interface (Figure 1b). A corresponding multivariate curve loading score plot of the electron energy loss spectroscopy exhibits a unique peak between EG and SiC, demonstrating the existence of the modified SiC layer (Figure 1c) signal. The existence of a 1–2 nm thick modified SiC layer was estimated independently from high-resolution cross-sectional TEM investigations (Figure 1a) and analysis of the ellipsometry spectra.

The measured VASE spectra, $\Delta(\omega)$ and $\Psi(\omega)$, for angles of incidence of 55°, 60°, and 65°, and the corresponding fit to the data, are plotted in Figure 2b,c respectively. The models fit the measured VASE spectra very well with a root mean square error of ≈ 1 . **Table 1** summarizes the parameters and models applied for each constituent material of the 2D metal heterostack. The utilized functions, all parameters and values for each constituent layer can be found in Table S2, Supporting Information. The (optically active) layer thickness from the VASE models are 0.49 ± 0.04 nm for 2D Ga and 0.46 ± 0.04 nm for 2D In, matching cross-sectional TEM.

2.2. Density Functional Theory Calculations

In order to explore the microscopic origin of the light–matter interaction of the 2D polar metals, we perform first principles DFT calculations using the plane-wave pseudopotential code, QUANTUM ESPRESSO,^[58] with the local density approximation (LDA)^[59] for the exchange–correlation functional. All calculation parameters are chosen to ensure convergence of the quantities of interest (see Methods Section). We model bilayer (2L) and trilayer (3L) Ga or In bonded to Si-terminated 6H SiC substrates, using slabs with six units of SiC per unit cell (**Figure 3**) (see Methods Section). Following previous studies on the energetically favored stacking configurations,^[42] the first (bottom) and the second Ga/In atomic layer are aligned, respectively, with the silicon atoms and carbon atoms in SiC1 (Figure 3), while for the trilayer, the third (top) atomic layer is aligned with the hollow sites of SiC1. The resulting interlayer distances are shown in Table S3, Supporting Information. The complex dielectric function is computed using the independent particle approximation^[60] (see Section S3, Supporting Information).

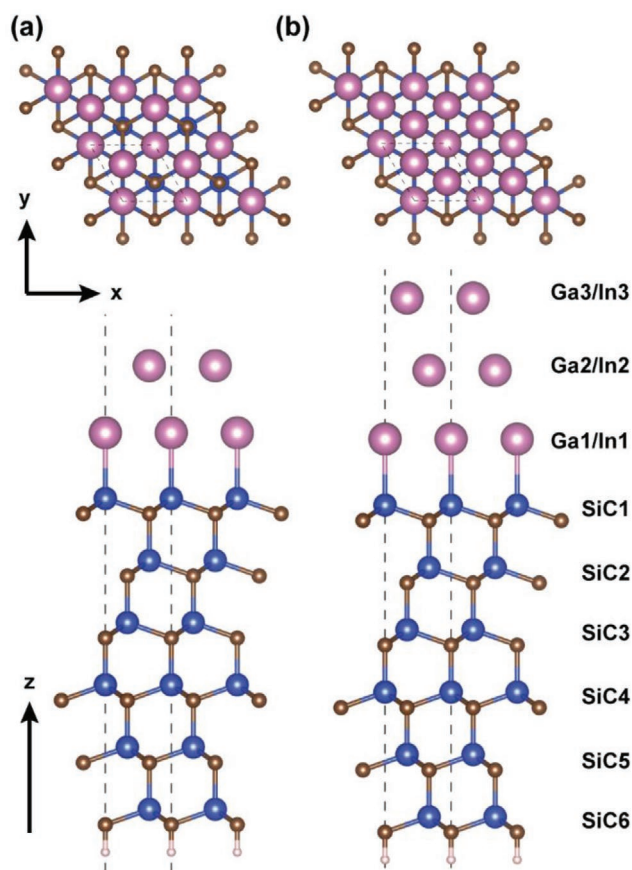


Figure 3. Atomic structures of half van der Waals 2D metals on SiC substrates. Top view and side view of the atomic structure of a) SiC/2L Ga or In, b) SiC/3L Ga or In. The SiC substrate is passivated by hydrogen atoms at the bottom.

The DFT band structure obtained for bilayer Ga/SiC (Figure 3a) agrees well with angle-resolved photoemission spectra (ARPES), except for the position of the Fermi level which is shifted by a few tenths of eV, consistent with the findings that graphene does not have a significant effect on the band structure.^[42] To investigate the effect of an error in the Fermi level on the predicted ε_2^{xx} , we shift the Fermi level in the calculations by ± 0.4 eV and ± 0.6 eV and present the results in Figure S4, Supporting Information. The results show that the peak positions above 1.0 eV are essentially unchanged by these Fermi level shifts.

2.3. Dielectric Functions

The experimentally extracted real and imaginary parts of dielectric functions $\varepsilon^{xx}(\omega) = \varepsilon_1^{xx}(\omega) + i\varepsilon_2^{xx}(\omega)$ are compared with DFT calculations in **Figures 4** and **5**, respectively. The free electron intraband contributions to $\varepsilon_1(\omega)$ are described by the Drude function as dashed lines in Figure 4a. A comparison of the absolute values of $\varepsilon_1(\omega)$ shows that the lowest investigated spectral region is dominated by the Drude term, that is, for $\omega_D(\text{Ga}) < 1$ eV for 2D Ga and $\omega_D(\text{In}) < 0.7$ eV for 2D In, respectively. The visible spectral range is dominated by a combination of a

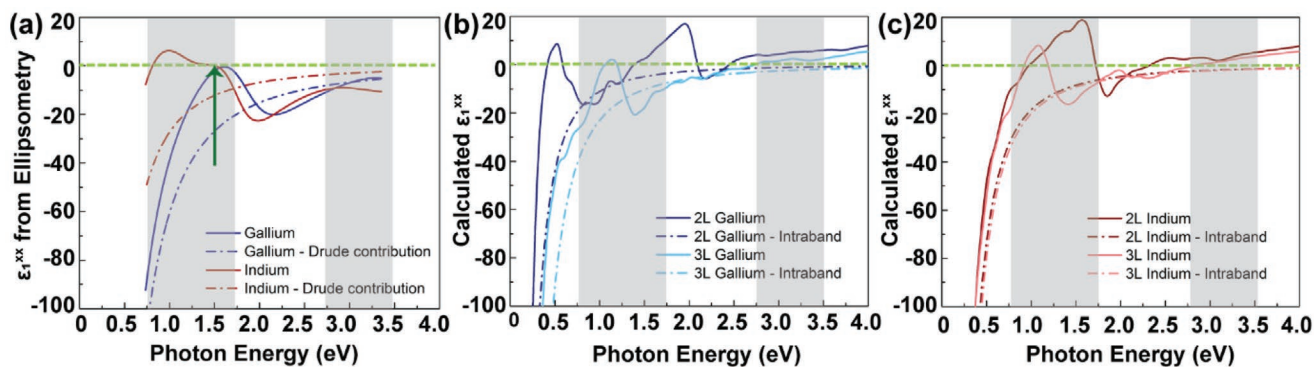


Figure 4. Real part of the complex dielectric function ϵ_1^{xx} . a) Real part of the complex dielectric function ϵ_1^{xx} obtained from fits to the spectroscopic ellipsometry data using the model defined in the text for 2D Ga and 2D In shown in blue and red, respectively. b) Calculated real part of the complex dielectric function ϵ_1^{xx} for 2L Ga (dark blue) and 3L Ga (light blue). c) Calculated real part of the complex dielectric function ϵ_1^{xx} for 2L In (dark red) and 3L In (light red). The isolated free electron intraband contributions are included as dash-dot lines for experimental data as well the calculated dispersions. The epsilon near zero (ENZ) spectral regions are highlighted in grey and the ENZ region around 1.5 eV by a green arrow.

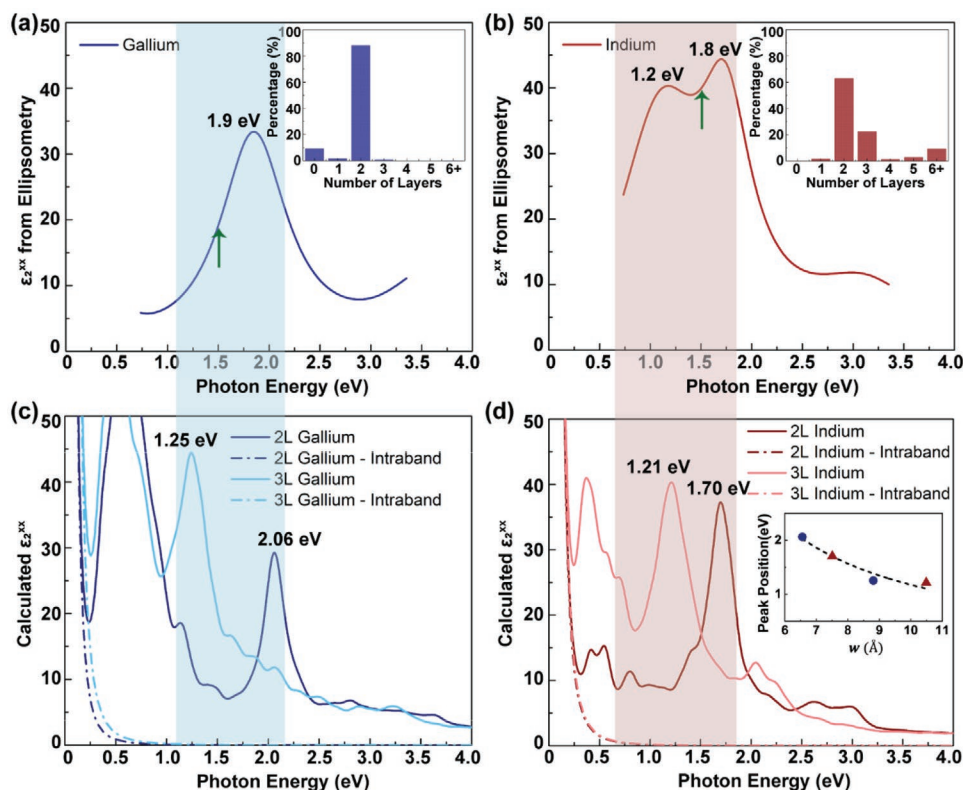


Figure 5. Imaginary part of the complex dielectric function ϵ_2^{xx} . a,b) Depict the imaginary part of the complex dielectric function ϵ_2^{xx} obtained from SE for 2D Ga and 2D In, respectively. The inset of (a) shows a statistical analysis of the number of 2D metal layers from several cross-sectional transmission electron micrographs. c,d) Depict the theoretically calculated imaginary part of the complex dielectric function ϵ_2^{xx} for 2D Ga and 2D In, respectively. These calculations are performed for 2L and 3L Ga and In. Resonances due to interband transitions are marked as well as the ENZ region in ϵ_1^{xx} around 1.5 eV. Comparison of (a) and (c) shows good agreement between the experimentally observed interband resonance at 1.9 eV with the resonance at 2.06 eV for 2L Ga indicating the dominance of bilayer Ga. This is in excellent agreement with the statistical analysis shown in the inset of (a) suggesting that Ga is predominantly 2L. Comparison of (b) and (d) shows good agreement of the experimentally observed interband resonance at 1.2 and 1.8 eV, and the theoretically calculated interband resonance at 1.21 eV for 3L and at 1.70 eV for 2L indicating the coexistence of 3L and 2L In, which is also in an excellent agreement with the statistical analysis shown in the inset of (b). The inset of panel (d) shows the calculated resonance energies as a function of layer number, that is, quantum confinement for Ga and In, respectively.

Tauc–Lorentz and two Lorentz functions for 2D In with peak energies of $\omega_{TL}(In) \approx 1.77$ eV and $\omega_{L1}(In) \approx 1.21$ eV, whereas the visible spectral range in 2D Ga is comprised of a single Tauc–Lorentz function with a peak energy of $\omega_{TL}(Ga) \approx 1.89$ eV. In the violet to UV spectral range, the dielectric functions are dominated by a combination of Drude and another Lorentz term with peak energies of $\omega_{L1}(Ga) \approx 3.62$ eV (out of experimental range, deciphered by fitting the obtained experimental data) and $\omega_{L2}(In) \approx 3.19$ eV for 2D Ga and 2D In, respectively. The amplitudes of the Tauc–Lorentz and the Lorentz oscillators are directly correlated with the loss function (extinction), and are high in the visible range, but significantly reduced in the violet to UV range. In this spectral range, the Drude term asymptotically pushes the real part $\epsilon_1(\omega) \rightarrow 0$. This higher energy ENZ region marked in grey in Figure 4, is predominantly due to the free electron contributions close to their plasmon resonance as known for metals.^[61] In this spectral region, the losses due to the bound electron contributions are also minimal, making this spectral range attractive for ENZ applications utilizing the properties of slow light and wavelength expansion.

The real part of the dielectric function $\epsilon_1(\omega)$ is near zero for 2D Ga at $\omega_{ENZ}(Ga) \approx 1.6$ eV, and even crosses $\epsilon_1(\omega) = 0$ twice for 2D In at $\omega_{ENZ1}(In) \approx 1.45$ eV and $\omega_{ENZ2}(In) \approx 0.82$ eV, in the red to NIR spectral region marked in Figure 4a. The losses are dictated by the magnitude of the imaginary part of the dielectric function $\epsilon_2(\omega)$ in Figure 5. Although the losses for 2D In in the red to NIR spectral range is large (Figure 5d), the losses for 2D Ga are lower by a factor of two for energies at the joint ENZ region centered around 1.5 eV. While high loss is unfavorable for applications like wave-guiding, light confinement or quantum plasmonics, other ENZ applications like efficient light absorber, hot-electron generation, photocatalysis, local heating, and nanoparticle trapping will benefit from the high losses.^[62–69] Most importantly, the light–matter interaction, ENZ properties, and related losses vary spectrally between 2D Ga and 2D In and are largely affected by quantum confinement (see inset of Figure 5d), indicating that controlling the number of layers and alloying these two materials would allow for introduction of a knob to tune the light–matter interaction. Furthermore, different metals and external stimuli such as gating or strain will allow for spectral tuning of the ENZ characteristic, a feature nearly impossible for their 3D metallic counterparts. Strain is expected to modify the quantum confinement and to alter the effective mass and electron–phonon coupling strength affecting the losses in the system, while gating is expected to impact the charge transfer characteristic, to presumably cause renormalization effects as well as to possibly modify the electron–electron and electron–phonon coupling strength.

The microscopic origin of the light–matter interaction of these 2D polar metals is explored via DFT calculations for in-plane real $\epsilon_1^{xx}(\omega)$ and imaginary $\epsilon_2^{xx}(\omega)$ parts of dielectric functions in Figures 4 and 5, respectively, with the free-electron intraband contributions plotted as dashed lines in Figure 4. A quantitative and qualitative agreement is seen between the experimentally observed dielectric spectra and the calculated values. DFT calculations show distinct energetic positions of the localized electron contributions for different metals and number of atomic metal layers. The influence of the broadening parameters in the calculation on the complex dielectric

function of 2L Ga is demonstrated in Figure S3, Supporting Information. Larger interband broadening results in broader and smoother features in $\epsilon_2^{xx}(\omega)$, but the peak positions are rather robust. Due to Kramers–Kronig relations, the shape of $\epsilon_1^{xx}(\omega)$ is determined by the actual values of $\epsilon_2^{xx}(\omega)$, and therefore changes with larger broadening. However, the computed $\epsilon_1^{xx}(\omega)$ is close to zero over a broad spectral range for all broadening parameters used here.

SE shows a strong interband resonance for 2D Ga at $\omega_{TL}(Ga) \approx 1.89$ eV, and a hint for a weaker resonance at $\omega_L(Ga) \approx 3.62$ eV (Figure 5a). DFT calculations for $\epsilon_2^{xx}(\omega)$ in bilayer Ga shows a distinct resonance at 2.06 eV, while trilayer Ga has a resonance at 1.25 eV. A comparison between experiment and theory suggests that the 2D Ga film is predominantly bilayer in nature. This is corroborated by statistical analysis from cross-sectional TEM micrographs shown in the inset of Figure 5a. SE of 2D In shows strong resonances at $\omega_{TL}(In) \approx 1.21$ eV and $\omega_{L1}(In) \approx 1.77$ eV, and a weak resonance at $\omega_{L2}(In) \approx 3.19$ eV (Figure 5b). The energetic positions of the strong resonances agree well with the calculated energies at 1.21 eV for trilayer In and 1.70 eV for bilayer In, while broad features are present at ≈ 2.6 – 3.0 eV for bilayer In. The characteristic energy positions of these calculated resonances and their dependence on the number of layers allow for the conclusion that the investigated 2D In sample is a mixture of bi- and trilayer regions. By comparing the ratio of the calculated loss intensities $\epsilon_2^{xx}(\omega)$ at 1.21 eV for trilayer In and 1.70 eV for bilayer with the measured intensity ratios of these peaks in the experimental data, we can estimate the amount of bi- and trilayer 2D In. Following this analysis, we estimate, based on peak intensities, that roughly 55% of the 2D In sample is bilayer and the rest trilayer. This is not too far from the statistical analysis from cross-sectional TEM micrographs shown in the inset of Figure 5b, and matches well with the predicted layer stability of 2D In.^[42] It is to be noted that we do not observe significant differences from the dielectric spectra from global VASE and spatially resolved SIE measurements (see Figure S2, Supporting Information) indicating that the distribution of bi- and trilayer regions is homogeneous. Therefore, the grain size of bi- and trilayers are expected to be below 1 μm .

While the free-electron intraband contributions are significant for $\epsilon_1^{xx}(\omega)$ over a large energy range, these intraband contributions decay quickly for $\epsilon_2^{xx}(\omega)$, and are small for energies larger than 0.75 eV. The characteristic resonance energies in $\epsilon_2^{xx}(\omega)$ discussed above arise from interband contributions. We analyze the microscopic origin of these resonance energies by projecting the states involved in the interband transitions onto specific atomic orbitals (see Section S3, Supporting Information). Figure 6a,b (and Figure S6a,d, Supporting Information) show that the main peaks in $\epsilon_2^{xx}(\omega)$ arise from transitions within the metallic states in each system. However, these peaks are present only for the SiC-supported 2D metals and not for the free-standing 2D metals (see Figure S7, Supporting Information). Charge transfer transitions involving both SiC and Ga/In states also contribute significantly to these optical absorption peaks, especially for the SiC1 (interface) layer, and to a lesser extent, the SiC2 layer (see Figure 3). Transitions within SiC also contribute to this peak while contributions of charge transitions between lower SiC units to Ga/In states are

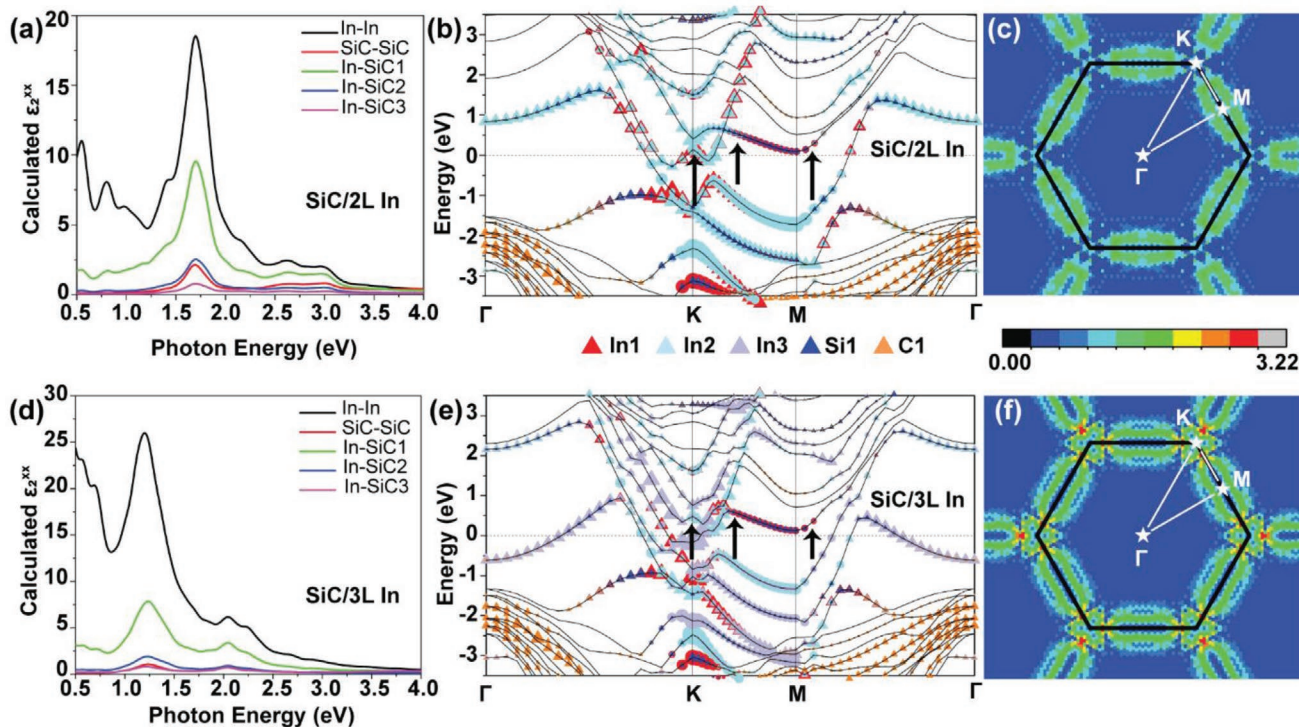


Figure 6. Analysis of interband transitions in SiC/2L In and SiC/3L In. $\epsilon_2^{\text{xx}}(\omega)$ of a) SiC/2L In and d) SiC/3L In arising from interband transitions between In states and In states, between SiC states and SiC states, and between In states and SiC states. The atomic layers for SiC follow the notation in Figure 3. Charge transfer transitions involving In and SiC layers SiC4, SiC5, and SiC6 yield negligible contributions to ϵ_2^{xx} and are omitted here. Electronic band structure for b) SiC/2L In and e) SiC/3L In. The colored symbols represent projections of the wavefunctions onto specific orbitals as shown in the legend. Arrows depict schematically interband transitions contributing to the main transition peaks. c, f) k -point-resolved ($\epsilon_2^{\parallel} = \epsilon_2^{\text{xx}} + \epsilon_2^{\text{yy}}$) within ± 0.1 eV of the main transition peak (b) at 1.70 eV SiC/2L In and (d) at 1.21 eV for SiC/3L In systems. High symmetry points Γ , K, and M are marked as white stars and the black hexagon is the boundary of the first BZ. The same color bar is used for both (c) and (f).

negligible. This analysis shows that the major peaks in $\epsilon_2^{\text{xx}}(\omega)$ arise primarily from interband transitions involving states of the 2D metal layer as well as the interface region. The energies of states primarily responsible for the interband transitions are also indicated in the partial density of states plots in Figure S5, Supporting Information, which further corroborates the finding that these transitions involve states localized on the metal layer and interface region.

The fact that the dielectric functions can be tuned by layer thickness (Figures 4 and 5) underlines the potential of designing from bottom-up the dielectric properties of these 2D polar metals. To understand why the major peaks in $\epsilon_2^{\text{xx}}(\omega)$ shift to lower energies going from bilayer to trilayer metals, we plot in Figure 6 the band structures as well as k -resolved values of ($\epsilon_2^{\parallel} = \epsilon_2^{\text{xx}} + \epsilon_2^{\text{yy}}$) for the major peaks in bilayer In and trilayer In systems. Similar results are shown in Figure S6, Supporting Information for bilayer Ga and trilayer Ga. In all systems, the interband transitions contributing to the major peaks arise primarily from the BZ boundaries (Figure 6c, f; Figure S6c, f, Supporting Information). Both the intensity of the k -resolved ϵ_2^{\parallel} and the region of k -space involved in the transitions increase when going from bilayer to trilayer, explaining the larger intensity predicted for the major peaks in the trilayer systems compared to bilayer ones. From the band structure plots, it is to be noted that the states involved in the interband transitions along K–M and close to K and M are dispersive states close to the Fermi

level. Arrows in Figure 6 and Figure S6, Supporting Information depict schematically these interband transitions. Along K–M, the transition involves an occupied state on the 2D metal, to an unoccupied state involving the metal and interface Si (Si1) layer. This observation is consistent with the discussion above, where interband transitions within the metal, and between the metal and SiC1 states were found to dominate the contribution to the major characteristic peaks in $\epsilon_2^{\text{xx}}(\omega)$. Transitions from Si1 to Si1 states can be seen close to the M point as well. We now explain the red-shift of major peaks in $\epsilon_2^{\text{xx}}(\omega)$ when going from bilayer to trilayer for the 2D SiC-supported metallic systems. Comparison of Figure 6b, e (as well as Figure S6b, e, Supporting Information) reveals that more metal layers result in more bands, which in turn have a smaller energy spacing along K–M and close to K and M points. These results can be qualitatively understood from the picture of confinement in a quantum well potential, where the energy spacing between quantum confined states decreases as the width of the well increases. Thus, the interband transitions discussed here will correspond to smaller transition energies for thicker metal films. Following the same quantum-mechanical confinement arguments, we can also explain the reduced energies of the resonances for 2D In as compared to 2D Ga, with the increased thickness of one atomic layer of In compared to Ga (see Table S3, Supporting Information). As shown in the inset of Figure 5d, the major peak positions ω_p computed for $\epsilon_2^{\text{xx}}(\omega)$ for Ga and In (2L and 3L systems)

decrease as the estimated effective width of the quantum well w increases. The best fit curve to these data points follows a relationship $\omega_p \approx w^{-1.3}$. The deviation of the fit from that expected for an infinite square well potential $\omega_p \approx w^{-2}$ is consistent with the important role of the interface between silicon carbide and the 2D metal in the interband transitions. Strong coupling of the metal wavefunctions to the silicon carbide substrate is expected to result in quantum tunneling out of the effective square well potential, thus reducing the confinement effect compared to that of an infinite square well. The fundamental understanding relating the thickness of the metal films to the major peak positions in $\epsilon_2^{\text{xx}}(\omega)$ serves as a guide to further tune both the real and imaginary parts of the dielectric functions in future work.

3. Conclusion

In summary, we have determined the frequency dependent in-plane complex dielectric functions $\epsilon^{\text{xx}}(\omega) = \epsilon_1^{\text{xx}}(\omega) + i\epsilon_2^{\text{xx}}(\omega)$ of atomically thin 2D In and 2D Ga layers hosted in half van der Waals heterostructures via combined theoretical and experimental approach utilizing DFT calculations and spectroscopic ellipsometry. The optical responses of these 2D metals are composed of electron contributions due to intraband excitations described by Drude functions and bound electron contributions due to different interband excitations described by Lorentzian functions. At lowest energies < 0.75 eV, and in the violet to UV range, the free electron contributions dominate the optical responses of the 2D metals. In the NIR to visible range however, the interband contributions govern the optical response. The resonance frequencies are characteristic of the number of atomic metal layers and choice of metal, allowing a high degree of tunability. Our developed approach allows for a rapid non-destructive determination of the thickness of the as-grown 2D polar metals. A quantum mechanical confinement effect is observed to act on the atomic orbitals forming the band structure, causing them to experience different confinement based on the number of atomic metal layers, analogous to quantum well structures. Therefore, energy separation of the underlying single particle bands is larger in bilayer compared to trilayer systems, but also for Ga layers compared to In due to the different thicknesses of each atomic monolayer. Both phenomena are confirmed experimentally. We observe the dependence of ENZ properties on the choice of metal and number of atomic metal layers in both the blue to UV region, and the NIR region, thus holding promise of the tunability of the ENZ spectral range. While the losses for bulk metals in the high energy ENZ region are small, the losses in the NIR regions and the technologically relevant telecommunication spectral region are large, again strongly dependent on the choice of metal and the number of atomic metal layers. Consequently, both the spectral range and the losses may be tunable by internal and external stimuli. These properties together with the possibility of their quantum mechanical tuning makes 2D polar metals in half van der Waals structures highly attractive for next generation plasmonics, quantum-plasmonics, and nano-plasmonic materials. These half van der Waals materials are fully integrable with other promising optically active 2D materials such as transition

metal dichalcogenides^[70] and their heterostructures,^[71–74] atomistic quantum emitters in 2D materials,^[75] and topologically non-trivial materials. Coupling with different material systems and (quasi-) particles therein, might result not only in field enhancement but in new quasiparticles such as chiral plasmons^[76] and plexitons.^[77,78] Strong light matter interaction in the non-linear^[79] as well as linear regime with ENZ properties found for these 2D polar metals is expected to result in fascinating and unprecedented phenomena facilitated by the unique properties of the 2D metals and their expected high tunability and integrability in photonic, plasmonic, and optoelectronic circuitries for next generation photonics, quantum plasmonics, hot-electron generation, photo-catalysis, solar power harvesting, sensing, and nano-particle trapping.^[62–69]

4. Experimental Section

Sample Preparation: A thermal vaporization-based method was used to intercalate the 2D Ga and 2D In at the epitaxial graphene/SiC interface.^[42] Epitaxial graphene was synthesized via high-temperature Si sublimation of SiC. Defects were then introduced in the graphene layers by exposing it to an O₂/He plasma. Following this treatment, 30–60 mg of Ga or In metal was placed in an alumina crucible along with the defective graphene sample in a Lindberg/Blue M Mini Mite tube furnace equipped with a 1" outer diameter quartz tube. The furnace is then heated to 600–800 °C under 300 Torr of argon and 50 sccm continuous argon flow for 30 min. This process yields metal intercalation at the epitaxial graphene/SiC interface.

EP4 Ellipsometry: Imaging spectroscopic measurements were implemented using a customized EP4 ellipsometer (Accurion GmbH). The data were obtained using the nulling ellipsometry mode in a spectral range of 480–1100 nm. The reflected light was focused with a 20× objective. The lateral resolution was in the order of a few μm by displaying the focused reflected light (objective with 20× magnification and an NA < 0.0018) on a CCD detector, enabling the micron-scale lateral resolution that allowed for investigating the homogeneities of the synthesized samples. The AOI is set at 50°. A razor blade edge was implemented as a beam cutter and set as close as possible to the sample surface to minimize the signal of backscattered light. 3–8 regions of interest were defined on the sample and measured under ambient conditions. The measurement method was EP4 nulling with a C-angle of 45° and a balanced quality, two zone or four zone measurement, two iterations and a P and A-angle range of ±10. The laser setting is set to power correction, which adjusts the laser output in reference to the power signal, and the camera was set to auto exposure. 100 datapoints were collected from 500–1100 nm and further 100–150 datapoints were collected from 500–900 nm.

VASE Ellipsometry: VASE were achieved using an M-2000 ellipsometer (J. A. Woollam) in rotating-compensator (RCE)-mode. The measurements were implemented at wavelengths ranging from 300 to 1700 nm, with the angle varied from 55° – 65° in five steps. Data were collected under ambient conditions in a clean room with a macroscopic laser spot size (≈1 mm). Each angle was assigned to an individual sample and in turn, each sample was assigned to one common dielectric function. Therefore, the obtained dielectric function was an average of the three angles.

The complex dielectric function $\epsilon(\omega) = \epsilon_1(\omega) + i\epsilon_2(\omega)$ and layer thickness d for each film of a measured layer stack can be extracted using the measured ellipsometric angles $\Psi(\omega)$ and $\Delta(\omega)$ as inputs to a Levenberg-Marquardt-fit based on the Berreman 4×4 matrix method for multilayered films.^[80] The obtained data was modeled using the EP4 modeling program (Accurion EP4 Model 3.6).

Transmission Electron Microscopy: Cross-sectional transmission electron microscopy samples were prepared by a Helios G4 PFIB UXe DualBeam with a Xe⁺ plasma ion source to avoid contamination from typical Ga

focused ion beam. A ≈ 500 nm carbon/platinum coating was deposited by the electron beam followed by a 50 nm thick layer of carbon at 5 keV and 6.4 nA. Then the Xe ion beam was used to deposit a 5 μm tungsten layer at 30 keV. A standard lift-out procedure was used and the samples were thinned down until they were transparent to a 5 keV electron beam. High-resolution STEM imaging of the prepared cross-sections was performed in an FEI Titan 80–300 HB Cubed transmission electron microscope equipped with a high-brightness gun (XFEG) and two spherical aberration correctors in both the probe and the image forming lenses. Several STEM-HAADF images were collected using an in-column Fischione detector at 63.8–200 mrad collection angles at 91 mm camera length and 19.1 beam convergence. The images were acquired at 200 keV with a screen current of 100 nA and 50 μm C2 aperture. A series of STEM images at 1.3 M \times are acquired along the cross-section of 2D Ga and 2D In samples with 2048 \times 2048 resolution and 2 μs pixel time. In all images, 10%–20% overlap was maintained between every image with both the previous and the next image to help to identify mutual fiducial markers from the carbon/platinum coating. Then, all the images were stitched manually to make a panorama image which was used to identify the number of Ga or In layers across the FIB cross-section and build the thickness histogram.

Low-Loss Electron Energy Loss Spectroscopy: Electron energy loss spectroscopy (EELS) was performed in the FEI Titan Krios operating at 300 kV and at liquid nitrogen temperature. The Krios was equipped with a GIF Quantum filter with two cameras behind the GIF including a Gatan ultrascan US1000XP and K2 direct electron detector. EELS spectra were collected on the K2 over a STEM image area of 66 \times 205 pixels with a pixel size of 0.2 nm at a magnification of 2.55 million. The GIF 5 mm entrance aperture was used and a dispersion on 0.1 eV over the energy loss range of 3–374 eV in order to record both low loss and core loss regions. In order to not overexpose the K2, the exposure time was set to the minimum of 0.0025 s and a shutter duty cycle of 20% is used. The total time to collect the spectrum image was 48 s. The EELS spectra was averaged across each row of the cross-section EELS image to help improve the S/N (0.2 \times 25 nm or 1 \times 125 pixels). A power law background was applied to remove the tail from the elastic scattering line. Multivariate Curve Resolution (MCR) decomposition analysis was applied to the averaged EELS spectra from each row.^[78] The accumulative percentage variation reached a maximum at 5 loadings (99.98%) and the loadings all correlated with identifiable features within the TEM cross-section (SiO₂ protective layer, EG, Ga, bright region of the SiC surface, and the SiC bulk).

Density Functional Theory Calculations: Density functional theory calculations were performed using the local density approximation (LDA)^[59] for the exchange-correlation functional as implemented in the plane-wave pseudopotential code, QUANTUM ESPRESSO.^[58] Optimized norm-conserving pseudopotentials^[81] were used to treat the electron-ion interactions. To obtain converged results, plane-wave kinetic energy cut-offs of 80 Ry and 90 Ry were used for 2D Ga/SiC and 2D In/SiC systems, respectively, and an energy threshold of 10^{−10} Ry was used for the self-consistent cycle. A Monkhorst–Pack k-point mesh of 26 \times 26 \times 1 was used for geometry optimization and self-consistent field calculations, while the density of states and dielectric functions were obtained using a denser k-point mesh of 52 \times 52 \times 1. The SiC slabs were modeled with six SiC units per unit cell, and dangling bonds at the bottom of the slab were passivated with hydrogen atoms. The bottom SiC unit was kept fixed while all other atomic positions were relaxed until the forces acting on the atoms were < 0.0001 Ry/Bohr. The theoretically predicted lattice constant for bulk 6H SiC ($a = 3.06$ Å) was used as the in-plane lattice parameter, which was in a good agreement with the experimental value of 3.08 Å.^[82] Periodic boundary conditions with an electrostatic dipole correction were used, with a vacuum length of 16 Å to separate periodic slabs. The complex dielectric function was computed using the independent particle approximation.^[60] In the sum over states, states with energies within ± 4 eV of the Fermi level for ϵ_2^{ab} were included. The results shown in this work were not changed when this energy window was widened. All valence states were involved in the computation of ϵ_1^{ab} and in total, 70 bands were considered for each system to get converged results. In the calculation of the complex dielectric function,

the intraband and interband broadening parameters were taken to be, respectively, 0.01 and 0.08 eV. Dependence of the complex dielectric functions on these broadening parameters is shown and discussed in Figure S3 and Section S3, Supporting Information.

Supporting Information

Supporting Information is available from the Wiley Online Library or from the author.

Acknowledgements

U.W., K.N., and A.W.H. acknowledge funding by the Deutsche Forschungsgemeinschaft (DFG, German Research Foundation) under Germany's Excellence Strategy – EXC 2089/1 – 390776260. S.S. and J.A.R. acknowledge the funding from NSF CAREER Award 1453924, NSF-DMR 2002651, and the Center for Nanoscale Science provided through the NSF Grant DMR-1420620. N.B. and J.A.R. acknowledge funding from Semiconductor Research Corporation Intel/Global Research Collaboration Fellowship Program, Task 2741.001, and 2D Crystal Consortium NSF Materials Innovation Platform under cooperative agreement DMR-1539916. W.H., K.A.U., and S.Y.Q. acknowledge funding from Grant NRF-NRFF2013-07 from the National Research Foundation, Singapore, and support from the Singapore National Research Foundation, Prime Minister's Office, under its medium-sized center program. Computations were performed on the NUS Graphene Research Centre cluster and National Supercomputing Centre Singapore (NSCC). H.E.S. and N.B. performed transmission electron microscopy work at McMaster University at the Canadian Centre for Electron Microscopy (CEEM), and were funded by AFOSR Award FA9550-19-1-0239 as well as the NSERC Discovery Grant program.

Open access funding enabled and organized by Projekt DEAL.

Conflict of Interest

The authors declare no conflict of interest.

Author Contributions

K.N., S.S., and W.H. contributed equally to this work. U.W. and J.R. designed the study. S.S. and N.B. prepared the samples and S.S. analyzed data. M.T.W., J.G., and H.E.S. provided cross-sectional TEM images and EELS. K.N. and M.L. performed spectroscopic ellipsometry measurement. K.N. implemented the model of the ellipsometry spectra. H.W., K.A.U., and S.Y.Q. performed the theoretical calculations and analysis. S.S., K.N., H.W., S.Y.Q., J.A.R., and U.W. wrote the paper with input from all co-authors.

Keywords

2D polar metals, dielectric properties, ellipsometry, epsilon near-zero, first principles calculations, half van der Waals structures, optical properties, quantum plasmonics

Received: July 15, 2020
Revised: October 4, 2020
Published online:

- [1] I. V. Bondarev, H. Mousavi, V. M. Shalaev, *Phys. Rev. Res.* **2020**, *2*, 013070.
- [2] P. Moitra, Y. Yang, Z. Anderson, I. I. Kravchenko, D. P. Briggs, J. Valentine, *Nat. Photonics* **2013**, *7*, 791.

- [3] N. Kinsey, M. Ferrera, V. M. Shalae, A. Boltasseva, *J. Opt. Soc. Am. B* **2015**, *32*, 121.
- [4] N. Kinsey, C. DeVault, A. Boltasseva, V. M. Shalae, *Nat. Rev. Mater.* **2019**, *4*, 742.
- [5] X. Niu, X. Hu, S. Chu, Q. Gong, *Adv. Opt. Mater.* **2018**, *6*, 1701292.
- [6] I. Liberal, N. Engheta, *Nat. Photonics* **2017**, *11*, 149.
- [7] D. C. Adams, S. Inampudi, T. Ribaud, D. Slocum, S. Vangala, N. A. Kuhta, W. D. Goodhue, V. A. Podolskiy, D. Wasserman, *Phys. Rev. Lett.* **2011**, *107*, 133901.
- [8] M. Silveirinha, N. Engheta, *Phys. Rev. Lett.* **2006**, *97*, 157403.
- [9] D. A. Powell, A. Alù, B. Edwards, A. Vakil, Y. S. Kivshar, N. Engheta, *Phys. Rev. B – Condens. Matter Mater. Phys.* **2009**, *79*, 245135.
- [10] H. Suchowski, K. O'Brien, Z. J. Wong, A. Salandrino, X. Yin, X. Zhang, *Science* **2013**, *342*, 1223.
- [11] N. Kinsey, C. DeVault, J. Kim, M. Ferrera, V. M. Shalae, A. Boltasseva, *Optica* **2015**, *2*, 616.
- [12] M. Z. Alam, I. De Leon, R. W. Boyd, *Science* **2016**, *352*, 795.
- [13] N. Kinsey, J. Khurgin, *Opt. Mater. Express* **2019**, *9*, 2793.
- [14] W. D. Newman, C. L. Cortes, J. Atkinson, S. Pramanik, R. G. Decorbey, Z. Jacob, *ACS Photonics* **2015**, *2*, 2.
- [15] I. I. Smolyaninov, V. N. Smolyaninova, A. V. Kildishev, V. M. Shalae, *Phys. Rev. Lett.* **2009**, *102*, 213901.
- [16] V. N. Smolyaninova, I. I. Smolyaninov, A. V. Kildishev, V. M. Shalae, *Appl. Phys. Lett.* **2010**, *96*, 211121.
- [17] T. S. Luk, S. Campione, I. Kim, S. Feng, Y. C. Jun, S. Liu, J. B. Wright, I. Brener, P. B. Catrysse, S. Fan, M. B. Sinclair, *Phys. Rev. B – Condens. Matter Mater. Phys.* **2014**, *90*, 085411.
- [18] A. I. Lvovsky, B. C. Sanders, W. Tittel, *Nat. Photonics* **2009**, *3*, 706.
- [19] K. L. Tsakmakidis, A. D. Boardman, O. Hess, *Nature* **2007**, *450*, 397.
- [20] T. Baba, *Nat. Photonics* **2008**, *2*, 465.
- [21] T. F. Krauss, *Nat. Photonics* **2008**, *2*, 448.
- [22] Y. Li, S. Kita, P. Munöz, O. Reshef, D. I. Vulis, M. Yin, M. Loncar, E. Mazur, *Nat. Photonics* **2015**, *9*, 738.
- [23] A. M. Mahmoud, I. Liberal, N. Engheta, *Opt. Mater. Express* **2017**, *7*, 1096.
- [24] A. Prain, S. Vezzoli, N. Westerberg, T. Roger, D. Faccio, *Phys. Rev. Lett.* **2017**, *118*, 133904.
- [25] M. Clerici, N. Kinsey, C. DeVault, J. Kim, E. G. Carnemolla, L. Caspani, A. Shaltout, D. Faccio, V. Shalae, A. Boltasseva, M. Ferrera, *Nat. Commun.* **2017**, *8*, 15829.
- [26] M. Z. Alam, S. A. Schulz, J. Upham, I. De Leon, R. W. Boyd, *Nat. Photonics* **2018**, *12*, 79.
- [27] S. Benis, P. Zhao, H. S. Pattanaik, D. J. Hagan, E. W. Van Stryland, Conf. on Lasers Electro-Optics, OSA publishing, San Jose, CA **2017**.
- [28] S. Benis, D. J. Hagan, E. W. Van Stryland, Conf. on Lasers Electro-Optics, OSA publishing, San Jose, CA **2018**.
- [29] A. M. Shaltout, M. Clerici, N. Kinsey, R. Kaipurath, J. Kim, E. G. Carnemolla, D. Faccio, A. Boltasseva, V. M. Shalae, M. Ferrera, Conf. on Lasers Electro-Optics, OSA publishing, San Jose, CA **2016**.
- [30] A. Ciattoni, C. Rizza, A. Marini, A. D. Falco, D. Faccio, M. Scalora, *Laser Photon. Rev.* **2016**, *10*, 517.
- [31] V. Caligiuri, M. Palei, G. Biffi, S. Artyukhin, R. Krahne, *Nano Lett.* **2019**, *19*, 3151.
- [32] N. Kinsey, C. DeVault, A. Boltasseva, V. M. Shalae, *Nat. Rev. Mater.* **2019**, *4*, 742.
- [33] M. N. Gjerding, M. Pandey, K. S. Thygesen, *Nat. Commun.* **2017**, *8*, 15133.
- [34] F. F. Zhu, W. J. Chen, Y. Xu, C. L. Gao, D. D. Guan, C. H. Liu, D. Qian, S. C. Zhang, J. F. Jia, *Nat. Mater.* **2015**, *14*, 1020.
- [35] M. Liao, *Nat. Phys.* **2018**, *14*, 344.
- [36] R. Sundararaman, T. Christensen, Y. Ping, N. Rivera, J. D. Joannopoulos, M. Soljačić, P. Narang, arXiv:1806.02672, **2018**.
- [37] Y. Zang, T. Jiang, Y. Gong, Z. Guan, C. Liu, M. Liao, K. Zhu, Z. Li, L. Wang, W. Li, C. Song, D. Zhang, Y. Xu, K. He, X. Ma, S. C. Zhang, Q. K. Xue, *Adv. Funct. Mater.* **2018**, *28*, 1802723.
- [38] M. S. Tame, K. R. McEnery, Ş. K. Özdemir, J. Lee, S. A. Maier, M. S. Kim, *Nat. Phys.* **2013**, *9*, 329.
- [39] T. C. Chiang, *AAPPS Bull* **2008**, *18*.
- [40] F. H. da Jornada, L. Xian, A. Rubio, S. G. Louie, *Nat. Commun.* **2020**, *11*, 1.
- [41] R. A. Maniyara, D. Rodrigo, R. Yu, F. J. Garcia de Abajo, V. Pruneri, J. Canet-Ferrer, D. S. Ghosh, R. Yongsunthon, D. E. Baker, A. Rezikyan, F. J. Garcia de Abajo, V. Pruneri, *Nat. Photon.* **2019**, *13*, 328.
- [42] N. Briggs, B. Bersch, Y. Wang, N. Nayir, R. J. Koch, K. Wang, M. Kolmer, W. Ko, A. D. L. F. Duran, S. Subramanian, C. Dong, J. Shallenberger, A. Bostwick, C. Jozwiak, E. Rotenberg, A.-P. Li, A. C. T. van Duin, V. Crespi, J. Robinson, *Nat. Mater.* **2020**, *19*, 637.
- [43] C. Yi, T. H. Kim, W. Jiao, Y. Yang, A. Lazarides, K. Hingerl, G. Bruno, A. Brown, M. Losurdo, *Small* **2012**, *8*, 2721.
- [44] F. K. Sculte, *Phys. Status Solidi* **1977**, *79*, 149.
- [45] Y. Chen, Z. Fan, Z. Zhang, W. Niu, C. Li, N. Yang, B. Chen, H. Zhang, *Chem. Rev.* **2018**, *118*, 6409.
- [46] A. Sinibaldi, N. Danz, E. Descrovi, P. Munzert, U. Schulz, F. Sonntag, L. Dominici, F. Michelotti, *Sensors Actuators, B Chem.* **2012**, *174*, 292.
- [47] X. Huang, S. Tang, X. Mu, Y. Dai, G. Chen, Z. Zhou, F. Ruan, Z. Yang, N. Zheng, *Nat. Nanotechnol.* **2011**, *6*, 28.
- [48] C. Gao, Z. Lu, Y. Liu, Q. Zhang, M. Chi, Q. Cheng, Y. Yin, *Angew. Chemie Int. Ed.* **2012**, *51*, 5629.
- [49] K. Yao, M. Salvador, C.-C. Chueh, X.-K. Xin, Y.-X. Xu, D. W. DeQuilettes, T. Hu, Y. Chen, D. S. Ginger, A. K. Y. A. Jen, *Adv. Energy Mater.* **2014**, *4*, 1400206.
- [50] D. Xu, X. Xiong, L. Wu, Y.-F. Xiao, *Adv. Opt. Photon.* **2018**, *10*, 706.
- [51] S. Funke, B. Miller, E. Parzinger, P. Thiesen, A. W. Holleitner, U. Wurstbauer, *J. Phys. Condens. Matter* **2016**, *28*, 385301.
- [52] U. Wurstbauer, C. Röling, U. Wurstbauer, W. Wegscheider, M. Vaupel, U. Wurstbauer, C. Röling, U. Wurstbauer, W. Wegscheider, *Appl. Phys. Lett.* **2010**, *97*, 231901.
- [53] C. Riedl, C. Coletti, T. Iwasaki, A. A. Zakharov, U. Starke, *Phys. Rev. Lett.* **2009**, *103*, 246804.
- [54] S. Mammadov, J. Ristein, R. J. Koch, *2D Mater.* **2017**, *4*, 015043.
- [55] P. Drude, *Ann. Phys.* **1900**, *306*, 566.
- [56] J. Mistrik, S. Kasap, H. E. Ruda, C. Koughia, J. Singh, *Springer Handbook of Electronic and Photonic Materials*, 2nd ed., Springer, Berlin **2017**.
- [57] H. Fujiwara, R. W. Collins, *Spectroscopic Ellipsometry for Photovoltaics: Fundamental Principles and Solar Cell Characterization*, Springer, Berlin **2018**.
- [58] P. Giannozzi, S. Baroni, N. Bonini, M. Calandra, R. Car, C. Cavazzoni, D. Ceresoli, G. L. Chiarotti, M. Cococcioni, I. Dabo, A. D. Corso, S. de Gironcoli, S. Fabris, G. Fratesi, R. Gebauer, U. Gerstmann, C. Gougoussis, A. Kokalj, M. Lazzeri, L. Martin-Samos, N. Marzari, C. Sbraccia, S. Scandolo, G. Sclauzero, A. P. Seitsonen, et al., *J. Phys. Condens. Matter* **2009**, *21*, 395502.
- [59] J. P. Perdew, Y. Wang, *Phys. Rev. B* **1992**, *45*, 13244.
- [60] P. Y. Yu, M. Cardona, *Fundamentals of Semiconductors; Graduate Texts in Physics*, Springer, Berlin **2005**.
- [61] D. Rioux, S. Vallières, S. Besner, P. Muñoz, E. Mazur, M. Meunier, *Adv. Opt. Mater.* **2014**, *2*, 176.
- [62] M. Moaied, M. M. A. Yajadda, K. Ostrikov, *Plasmonics* **2015**, *10*, 1615.
- [63] C. David, N. A. Mortensen, *J. Christensen, Sci. Rep.* **2013**, *3*, 1.
- [64] S. Raza, T. Christensen, M. Wubs, S. I. Bozhevolnyi, N. A. Mortensen, *Phys. Rev. B – Condens. Matter Mater. Phys.* **2013**, *88*, 115401.
- [65] H. Chalabi, D. Schoen, M. L. Brongersma, *Nano Lett.* **2014**, *14*, 1374.
- [66] B. Hou, L. Shen, H. Shi, R. Kapadia, S. B. Cronin, *Phys. Chem. Chem. Phys.* **2017**, *19*, 2877.
- [67] M. L. Juan, M. Righini, R. Quidant, *Nat. Photon.* **2011**, *5*, 349.
- [68] M. L. Juan, R. Gordon, Y. Pang, F. Eftekhari, R. Quidant, *Nat. Phys.* **2009**, *5*, 915.

- [69] J. C. Ndukaife, A. V. Kildishev, A. G. A. Nnanna, V. M. Shalae, S. T. Wereley, A. Boltasseva, *Nat. Nanotechnol.* **2016**, *11*, 53.
- [70] J. Sun, H. Hu, D. Zheng, D. Zhang, Q. Deng, S. Zhang, H. Xu, *ACS Nano* **2018**, *12*, 41.
- [71] S. Subramanian, Q. T. Campbell, S. Moser, J. Kiemle, P. Zimmermann, P. Seifert, F. Sigger, D. Sharma, H. Al-Sadeg, M. Labella, D. Waters, R. M. Feenstra, R. J. Koch, C. Jozwiak, A. Bostwick, E. Rotenberg, I. Dabo, A. Holleitner, T. E. Beechem, U. Wurstbauer, J. A. Robinson, arXiv: 2006.14689, **2020**.
- [72] S. Subramanian, K. Xu, Y. Wang, S. Moser, N. A. Simonson, D. Deng, V. H. Crespi, S. K. Fullerton-Shirey, J. A. Robinson, *npj 2D Mater. Appl.* **2020**, *4*, 9.
- [73] N. Briggs, S. Subramanian, Z. Lin, X. Li, X. Zhang, K. Zhang, K. Xiao, D. Geohegan, R. Wallace, L.-Q. Chen, M. Terrones, A. Ebrahimi, S. Das, J. Redwing, C. Hinkle, K. Momeni, A. van Duin, V. Crespi, S. Kar, J. A. Robinson, *2D Mater.* **2019**, *6*, 022001.
- [74] S. Subramanian, D. D. Deng, K. Xu, N. Simonson, K. Wang, K. Zhang, J. Li, R. Feenstra, S. K. Fullerton-Shirey, J. A. Robinson, *Carbon N. Y.* **2017**, *125*, 551.
- [75] J. Klein, M. Lorke, M. Florian, F. Sigger, L. Sigl, S. Rey, J. Wierzbowski, J. Cerne, K. Müller, E. Mitterreiter, P. Zimmermann, T. Taniguchi, K. Watanabe, U. Wurstbauer, M. Kaniber, M. Knap, R. Schmidt, J. J. Finley, A. W. Holleitner, *Nat. Commun.* **2019**, *10*, 2755.
- [76] M. Hentschel, M. Schäferling, X. Duan, H. Giessen, N. Liu, *Sci. Adv.* **2017**, *3*, e1602735.
- [77] Y. Zakharko, M. Rother, A. Graf, B. Hähnlein, M. Brohmann, J. Pezoldt, J. Zaumseil, *Nano Lett.* **2018**, *18*, 4927.
- [78] M. Held, A. Graf, Y. Zakharko, P. Chao, L. Tropic, M. C. Gather, J. Zaumseil, *Adv. Opt. Mater.* **2018**, *6*, 1700962.
- [79] M. A. Steves, Y. Wang, N. Briggs, T. Zhao, H. El-Sherif, B. Bersch, S. Subramanian, C. Dong, T. Bowen, K. Nisi, M. Lassaunière, U. Wurstbauer, N. Bassim, J. J. Fonseca, J. T. Robinson, V. Crespi, J. Robinson, K. L. Knappenberger, arXiv: 2004.01809, **2020**.
- [80] D. W. Berreman, *Opt. Soc. Am.* **1972**, *62*, 502.
- [81] D. R. Hamann, *Phys. Rev. B – Condens. Matter Mater. Phys.* **2013**, *88*, 085117.
- [82] A. Bauer, J. Kräußlich, L. Dressler, P. Kuschnerus, J. Wolf, K. Goetz, P. Käckell, J. Furthmüller, F. Bechstedt, *Phys. Rev. B – Condens. Matter Mater. Phys.* **1998**, *57*, 2647.